Dynamic Wall Shear Stress Measurement using Event-based 3D Particle Tracking

C. Willert[1,*], J. Klinner[1]

1: DLR Institute of Propulsion Technology, German Aerospace Center, Germany
*Corresponding author: chris.willert@dlr.de

Keywords: fluid flow measurement, turbulence, turbulent boundary layer, shear stress measurement, particle imaging, event-based imaging, dynamic vision sensor, particle tracking, PTV.

ABSTRACT

We describe the implementation of a 3d Lagrangian particle tracking (LPT) system based on event-based vision (EBV) and demonstrate its application for the near-wall characterization of a turbulent boundary layer (TBL) in air. The viscous sublayer of the TBL is illuminated by a thin light sheet that grazes the surface of a glass window inserted into the flat wall of the wind tunnel wall. The data simultaneously captured by three synchronized event-cameras is used to reconstruct the 3d particle tracks within $400\,\mu\mathrm{m}$ of the wall on a field of view of $12.0\,\mathrm{mm} \times 7.5\,\mathrm{mm}$. The velocity and position of particles within the viscous sub-layer permit the estimation of the local, unsteady wall shear stress vector under the assumption of linearity between particle velocity and wall shear stress. Thereby, 2d distributions and higher order statistics of the unsteady wall shear stress are obtained. The employed EBV hardware coupled with suited LPT tracking algorithms provide data quality on par with currently used, considerably more expensive, high-speed framing cameras.

1. Introduction

EBV, also termed *dynamic vision sensing* (DVS), is a new upcoming field within the field of computer vision. For a recent review of the technology and underlying concepts the reader is referred to the topical review by Gallego et al. (2022). In short: Contrary to conventional frame-based imaging, EBV only records changes of image intensity (i.e. contrast changes) on the pixel level, triggering a positive event ($+1$) for increasing intensity and a negative event (-1) for a decreasing intensity change. The typical threshold of the intensity-change trigger is on the order of 10–20% but can be fine tuned. As the pixels on the detector respond individually, the events appear asynchronously throughout the detector area resulting in a continuous stream of data, with each event datum $E_i = E_i(\mathbf{x}, t, p)$ consisting of pixel coordinates $\mathbf{x_i} = (x_i, y_i)$, a time stamp t_i and a polarity $p_i \in \{+1, -1\}$ indicating the direction of the intensity change.

After original prototype and conceptual development of the technology in 1990's, affordable and ready-to-use hardware based on EBV only recently have become available with current sensor resolutions of 1 MPixel. This has broadened the range of applications as testified in a steadily increasing number of publications (see e.g. Robotics and Perception Group, 2023).

The application of EBV for the visualization and measurement of fluid flows is by no means new. Initial work was performed by Drazen et al. (2011) on particle tracking velocimetry (PTV) of dense particles in a solid–liquid two-phase pipe flow using an EBV sensor of 256×256 pixels and continuous laser (5W) illumination. Ni et al. (2012) used an EBV array of 128×128 elements to demonstrate micro-particle tracking (μPTV) with $12\,\mu\mathrm{m}$ microspheres and were able to detect Brownian motion. Using a stereoscopic EBV system, Wang et al. (2020) implemented a 3d PTV system allowing them to reconstruct three-dimensional tracks with 2d tracking results from camera. Their flow experiment consisted of a small hexagonal cell with stirrer inducing a swirling flow containing O($100\,\mu\mathrm{m}$) polystyrene spheres. First PTV measurements in an air flow were performed by Borer et al. (2017) using three synchronized EBV cameras (128×128 pixels) to track helium filled soap bubbles (HFSB) in volumes up to about 1 m side length using white light LED arrays for illumination. The flow was only sparsely seeded allowing individual particles to be tracked with final data sets containing up to O(1 000 - 10 000) tracks. More recently, Rusch & Rösgen (2023) re-implemented this concept as a real-time 3d PTV system enabling live flow field reconstruction.

The work presented herein extends upon the recently introduced event-based imaging velocimetry (EBIV) concepts (Willert, 2023; Willert & Klinner, 2022) and introduces a 3d-3c particle tracking system in a macroscopic imaging configuration with a magnification approaching unity. In comparison to previous implementations, much higher seeding densities are achieved. However, due to the high data load, the captured event data sequences currently can only be processed in an off-line fashion, that is, after completion of the measurement. The setup is used to acquire the near wall trajectories of tracers within the viscous sublayer, specifically to estimate the unsteady wall shear stress (WSS).

2. 3d-3c Tracking System

The 3d-3c particle tracking system comprises a triplet of event cameras in a photogrammetric configuration, that is, arranged in a manner to capture a common, relatively thin volume of interest. Scheimpflug mounts on the off-normal cameras allow a common plane of focus for all three cameras (Fig. 1). The set of 3 cameras are synchronized with an external 1 MHz source to ensure common a time-base. In addition, reference pulses at 100 Hz allow precise alignment of the recorded event records with a resolution of $1\,\mu\mathrm{s}$ with respect to each other (c.f. Fig. 2).

In the present application, the tracking system is mounted below the wind tunnel section and observes the bottom layer of the TBL through a 1 mm thin glass window with anti-reflective coating.

This domain is illuminated with a ≈ 0.5 mm thin light sheet introduced from the side of the wind tunnel with a slight inclination ($\approx 0.5°$, c.f. Fig. 1b). The light sheet is oriented such that all cameras receive the light scattered by the tracers at a common scattering angle of $90°$. This results in similar illumination intensities on all three detectors.

At a working distance of about 200 mm a common field of view (FOV) of about $12.0 \times 7.5\,\mathrm{mm}^2$ is captured (magnification $m = 0.48$ with $10\,\mu\mathrm{m}$/pixel). The pulsed laser (Innolas Nanio-Air) is operated at pulsing frequencies of 5 kHz or 10 kHz with an integral power of about 1–2 W and is synchronized to the camera time base (see Fig. 2). The macro objective lenses (Nikon Micro-Nikkor 55 mm / 2.8) are stepped down to $f_\# = 8$.

Water-based tracer particles of about $1 - 2\,\mu\mathrm{m}$ and a life-time of about 10 minutes are provided by a fog generator (HazeBase Classic with base*M fluid). Event-recordings of up to 60 s duration are acquired at wind tunnel speeds of $U_\infty = 5.2, 7.5$ and 10 m/s. Recordings at different seeding concentrations and detector region of interest (ROI) allow an assessment tracking system performance.

Fig. 3 intends to provide an impression of the event data acquired by one of the camera at two different seeding concentrations. Keeping the laser energy and light sheet position constant, the seeding density is varied by about one order of magnitude.

(a) (b)

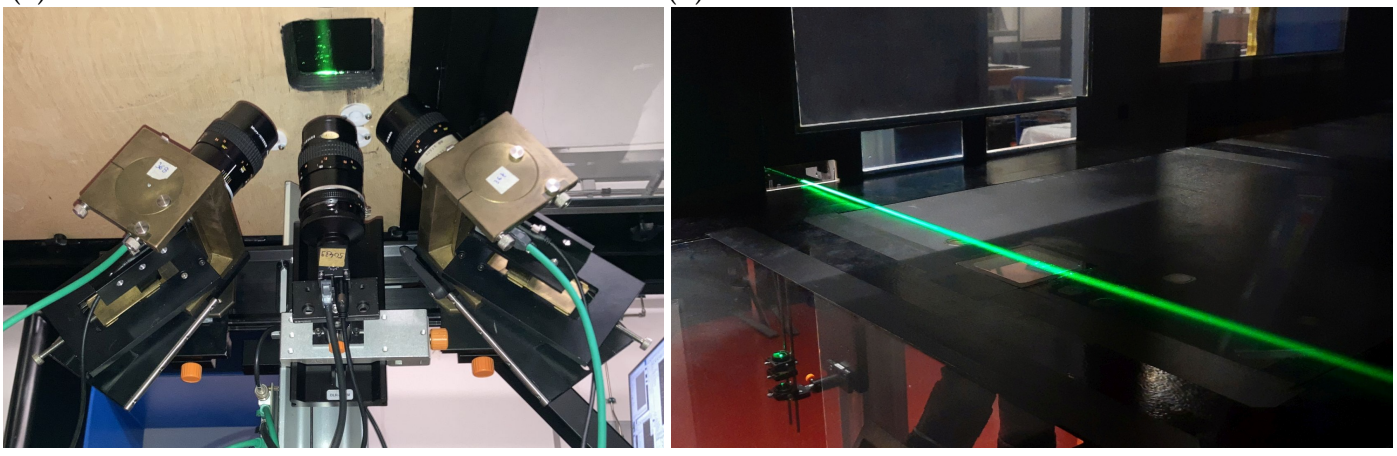

Figure 1. Triple event-camera setup placed below the 1 m wind tunnel of DLR in Göttingen for particle tracking in the viscous sublayer of a TBL, (b) laser light sheet grazing the window at the observation area at an estimate angle of $\approx 0.5°$ to the surface.

3. Camera calibration

Elemental for reliable 3d-PTV is an accurate camera mapping which allows a transformation from image space into object space and back. This is generally achieved using established camera calibration procedures.

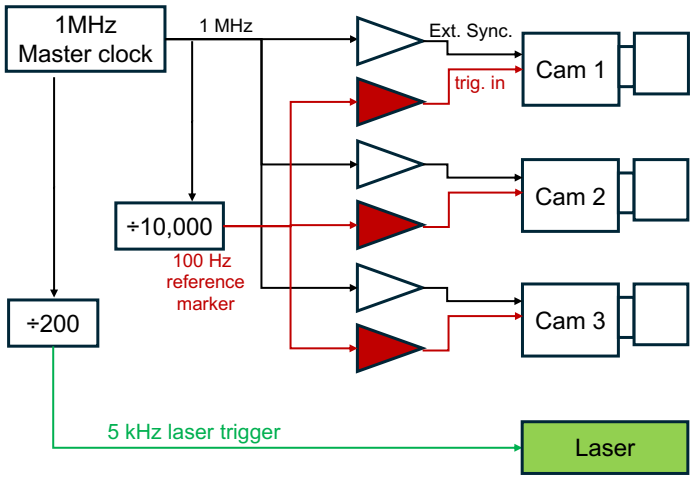

Figure 2. Synchronization unit provides common time base for all event cameras as well as laser trigger.

(a)

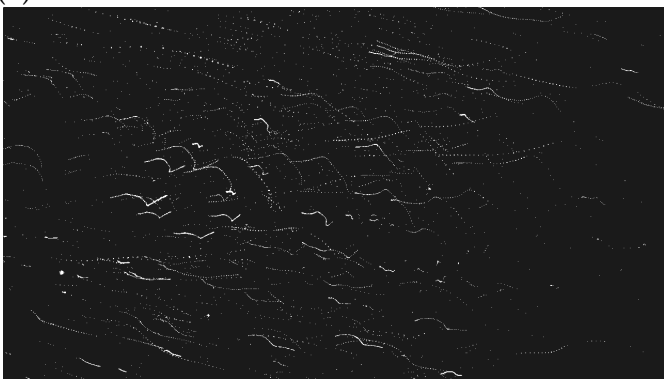

(b)

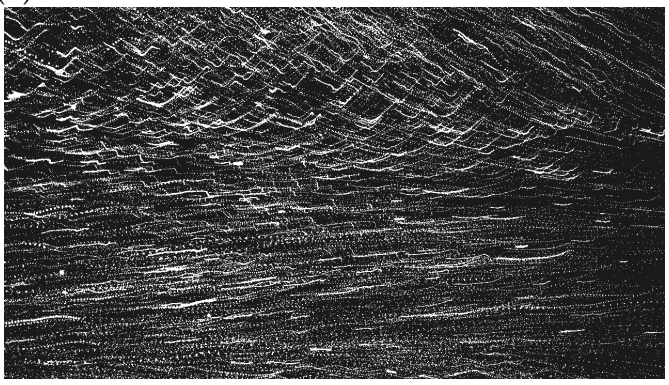

Figure 3. Sample pseudo-images from $10\,\mathrm{ms}$ of the event stream recorded by the central camera at $1.4\,\mathrm{Mev/s}$ (a) and $22\,\mathrm{Mev/s}$ (b). With a laser pulse rate of $5\,\mathrm{kHz}$, the pseudo-images contain 50 laser pulses.

Calibration data in the form of image-object correspondence points is collected from recordings of a calibration target. Here, a checker-board target with $1\,\mathrm{mm} \times 1\,\mathrm{mm}$ squares printed on glass is mounted parallel to the observation window and traverse in wall-normal (y) direction at increments of $\Delta y = 250\,\mu\mathrm{m}$ (Fig. 4a). Due to insensitivity of the EBV to static imagery, the glass target is back-illuminated by a pulsed LED at $100\,\mathrm{Hz}$. Summing events over period of $0.5\,\mathrm{ms}$ provides high-contrast calibration images suitable for grid marker detection (Fig. 4b). The common FOV shared by the cameras is depicted in Fig. 5 and extends about $12\,\mathrm{mm}$ by $7.5\,\mathrm{mm}$, respectively in streamwise and spanwise direction.

The accuracy of particle reconstruction in relation to the glass surface requires the knowledge of plane spanned by the target in relation to the plane of glass surface. This is achieved by triangulation of stationary particles and dust attached to the surface, which are readily detected in the raw event data as continuous triggered pixel clusters. A 2d plane fit provides the reference plane to which the reconstructed track data will be aligned (Fig. 5b). The slope amounts to about $50\,\mu\mathrm{m}$ across the $10\,\mathrm{mm}$ FOV (inclination $\approx 0.3°$).

A dual plane method is used to map between object and image space and to compute epipolar lines to match the particle images between the views. A particle-based residual alignment such as typically performed in 3d "Shake the Box" (STB) LPT is currently not employed.

(a) 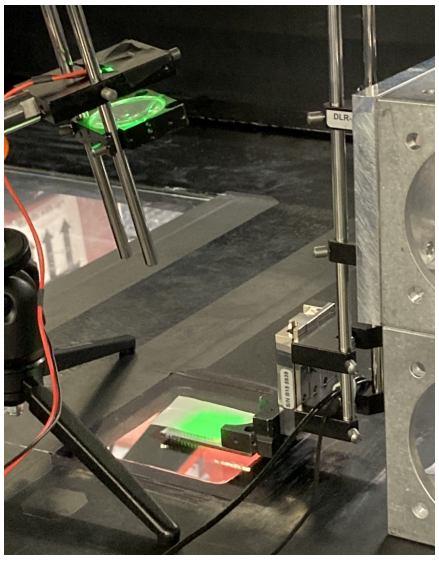 (b) 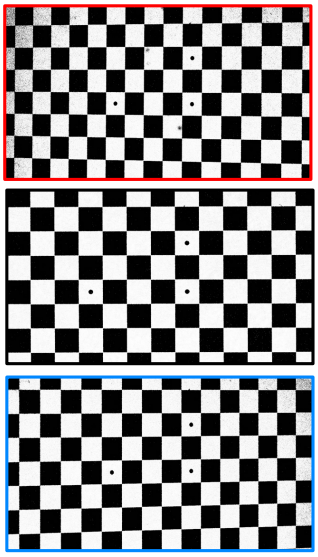

Figure 4. Camera calibration setup using a back-illuminated checker-board target mounted on a micro-translation stage (a), simultaneous camera views of the target (b).

4. Event-data processing

Prior to particle tracking, the acquired event-recordings are temporally aligned using the external 100 Hz reference markers and then converted to pseudo-image sequences by re-sampling the event-data at a frequency corresponding to the laser pulsing rate. During a sample interval, e.g. $200\,\mu s$ at $5\,kHz$ laser pulsing, any given pixel is only allowed to produce at most one event. Hence, the resulting pseudo-image is binary in nature. The automated event-sampling is performed on the basis of searching for the minimum in the ensemble averaged event stream, a representative example of which is given in Fig. 6 for a laser pulsing frequency of $5\,kHz$. In this, case the sampling period, as indicated by the red dashed lines, would begin with an offset of $\approx 175\,\mu s$ and ends $200\,\mu s$ later. Further details and the motivation for the pulsed illumination technique are described in Willert (2023).

Particle tracking is performed for each camera view individually by first extracting contiguous binary pixel blobs from the pseudo images and computing their centroids (center of mass). A k-d tree based nearest-neighbor search scheme (KNN) then detects tracklets across three adjacent pseudo-images and extends these via a predictor scheme to the following image frames. The tracker accepts gaps of up to one pseudo-frame to link tracks of particle images that approach the detection threshold. Reconstruction of the 3d tracks is performed using epipolar lines of a given particle on the other two views. Finally, a least-squares regression is applied to the reconstructed tracks to estimate a given particle's position, velocity and acceleration along its path.

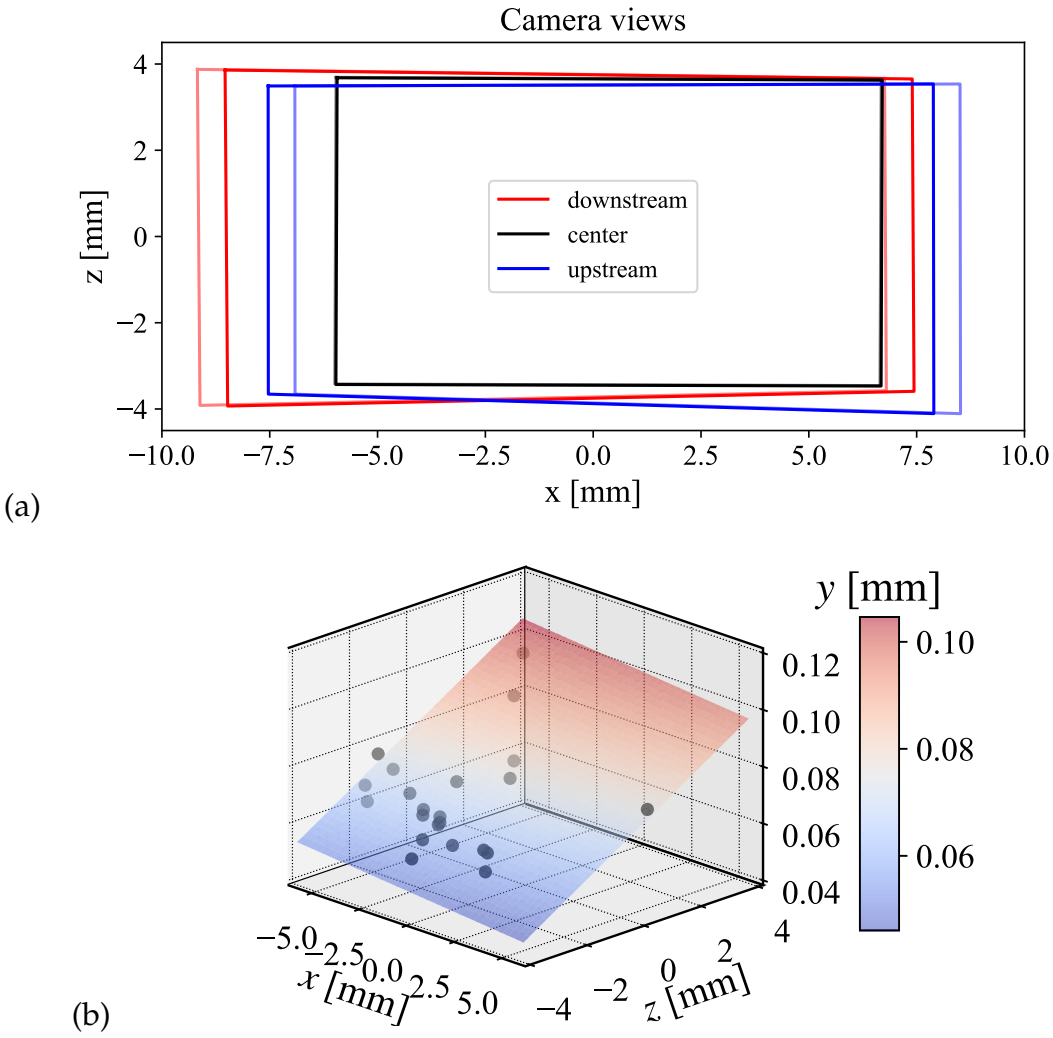

Figure 5. Camera field of view at $y = 0$ and $y = 500\,\mu\text{m}$ (a). Reconstructed plane of the glass insert based on 3d reconstruction of stationary particles stuck to the surface (b).

Instantaneous particle velocity is estimated using an incremental second order polynomial fit on the particle track segments of length $N = 5$. Validation is based on the residuals of the 3d track reconstruction and the residuals of the least squares track fit. The wall shear stress vector $\vec{\tau}_w = [\tau_{w,x}, \tau_{w,z}]$ for each validated particle position is then obtained be dividing its estimated velocity $\mathbf{u} = [u, w]$ by its distance from the wall Δy as an approximation to the definition of WSS

$$\vec{\tau}_w = \mu \left.\frac{\partial \mathbf{u}}{\partial y}\right|_{y=0} \approx \mu \frac{\mathbf{u}(\Delta y)}{\Delta y} \tag{1}$$

with μ representing the dynamic viscosity and the range of Δy limited the viscous layer ($y^+ < 5$).

Fig. 7 shows two realizations of recovered near-wall tracks at $U_\infty = 5.2$. The particle positions are color-coded with the mean wall stress magnitude $\|\vec{\tau}_w\|$ with the mean value gray-colored. While the tracks in Fig. 7(a) indicate a low-shear condition and even some flow reversal, the flow topol-

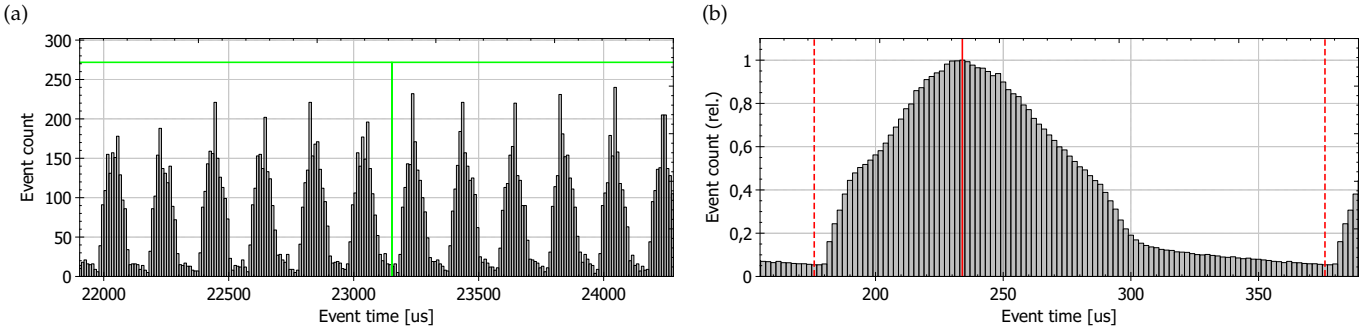

Figure 6. Histograms of positive event data recorded by one of the three cameras with the laser pulsing at 5 kHz, green line indicates 1 µs reference marker at 100 Hz used for registration of event streams to one another; (a) raw stream binned at 10 µs intervals, (b) mean event distribution during one pulsing period (200 µs).

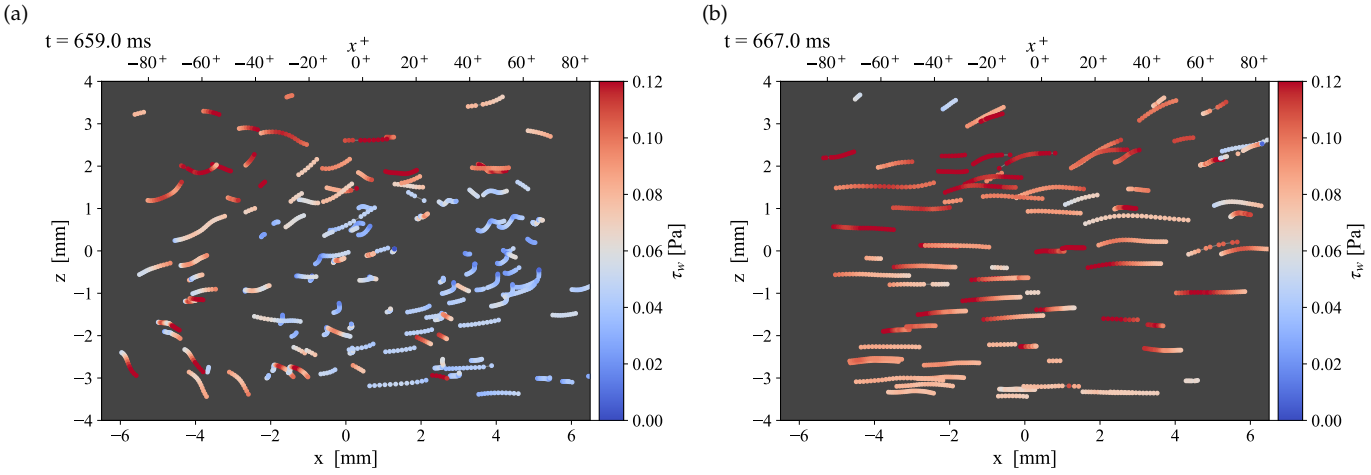

Figure 7. Processed particle tracks color coded with wall shear stress magnitude at $\mathrm{Re}_\tau = 585$. Each frame represents 5 ms of event-data (25 light pulses). The mean flow direction is from left to right.

ogy is completely different only 8 ms later (Fig. 7b) when it is dominated by high shear rate aligned with the mean flow direction. The shear rate partially exceeds the mean value by a factor of two.

4.1. Mean velocity profile and statistics

Profiles of mean particle velocity and associated higher moments are compiled by bin-averaging across the FOV at different wall distances y_i. Fig. 8 presents profiles obtained with a bin width of $\Delta y = 1\,\mu\mathrm{m}$. The mean streamwise profile (Fig. 8a) is in good agreement with the DNS up to a wall distance of $y \approx 400\,\mu\mathrm{m}$ beyond which it begins to deviate. The deviation is believed to be sourced in the under-representation of faster particle tracks in the statistics: at a velocity of $U = 1\,\mathrm{m/s}$ the particles move by $20\,\mathrm{pixel}$ between laser shots, with faster moving particles less likely to be tracked. For the present data set useful velocities are available up to a wall distance $y+ \approx 4 - 5$.

The slope of the mean profile in a range $50\,\mu\mathrm{m} \leq y \leq 200\,\mu\mathrm{m}$ is a used for the estimation of the

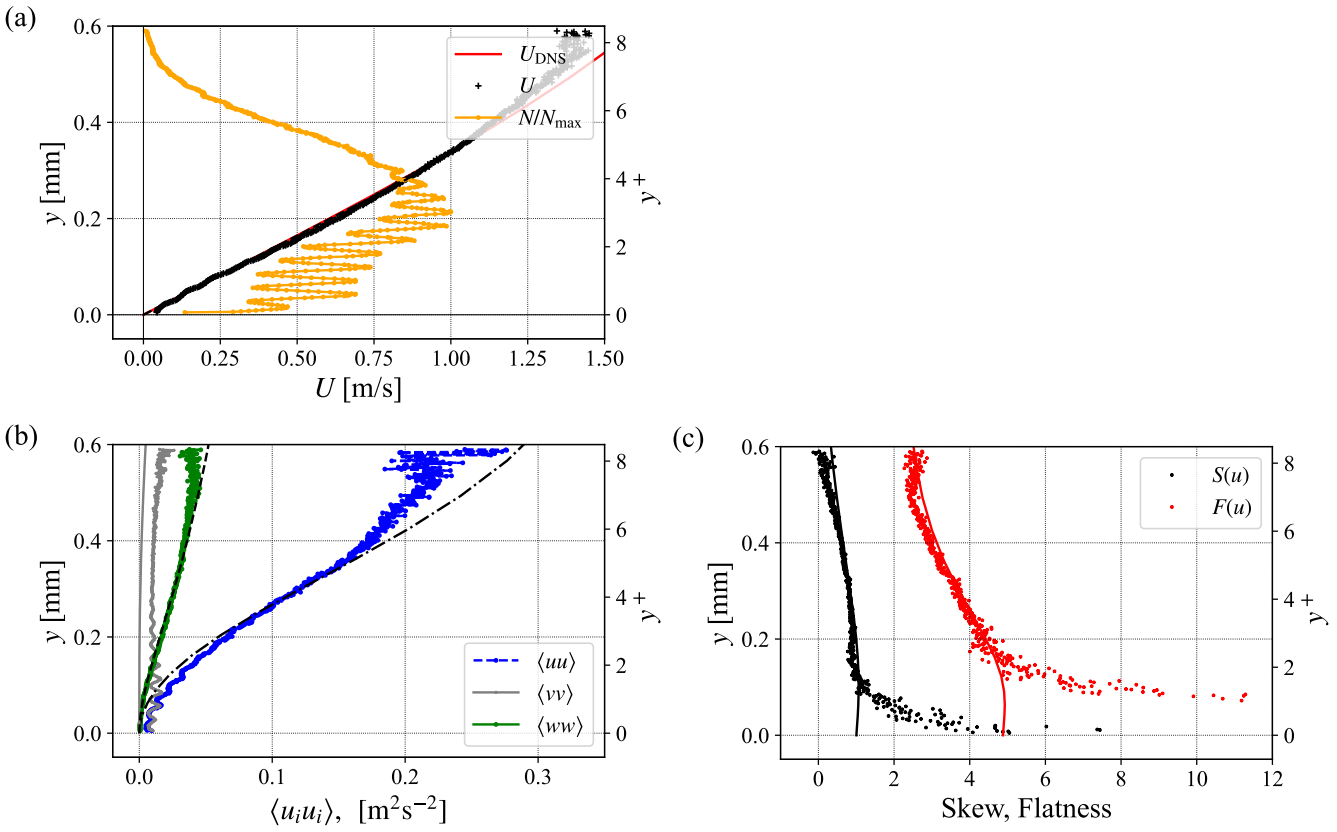

Figure 8. Bin-averaging results using $\Delta_y = 1\,\mu\text{m}$ bins: (a) near-wall velocity profile (+) and DNS prediction (red line). Orange line represent the relative sample count N_i of the bins; (b) velocity variances for streamwise (blue), spanwise (green) and wall-normal (+) components; (c) skewness S_{τ_x} and kurtosis F_{τ_x} estimates in comparison to DNS predicted values (solid lines). DNS from Schlatter & Örlü (2010).

mean velocity gradient at the wall, $\partial u/\partial y|_{y=0}$, which in turn is required in (Eq. 1) to estimate the mean WSS, $\bar{\tau}_w$, alongside with the estimation of the viscous scaling $l^* = \nu/u_\tau$.

The variances of all three components of the velocity vector are plotted in Fig. 8(b) and are in good agreement with DNS up to a wall distance of $y^+ \approx 5$ ($330\,\mu\text{m}$). The variance of the wall-normal component $\langle vv \rangle$ is a constant level throughout indicating noise. With near-wall flow essentially restricted to be only wall-parallel, track validation can rely on limiting the variance and magnitude of the wall-normal component (see also Fig. 13c).

Finally, Fig. 8(c) provides the third and fourth order moments, i.e. skewness S_u and kurtosis F_u of the streamwise velocity. These line up with DNS prediction for wall distances $y^+ > 2$ but strongly deviate closer to the wall, indicating an increased amount of erroneous data near the wall, the net effect of which is averaged out in both the mean as well as the variances. The cause for the deviation is not yet fully resolved.

In addition to the mean velocity profile, Fig. 8(a) also provides the relative sample count within each of the $1\,\mu\text{m}$ bins (orange line). In a region of $0 < y < 300\,\mu\text{m}$ this value modulates at a spatial

frequency of $\Lambda = 24.0\,\mu\mathrm{m}$ and can be explained by an intensity modulation within the laser light sheet which is reflected by the glass surface as its grazes it at a shallow angle. The spacing of the interference fringes Λ is related to the incidence angle θ by

$$\Lambda = \frac{\lambda}{2\sin(\theta)} \tag{2}$$

where λ is the wavelength of the laser light ($532\,\mathrm{nm}$). The estimated angle of $\theta = 0.635°$ matches the $5\,\mathrm{mm}$ entry height of the laser beam at the side of the tunnel. With the fringes restricted to the lower $300\,\mu\mathrm{m}$ the first incidence of the laser beam with the surface is estimated to be located about $25 - 30\,\mathrm{mm}$ away from the measurement volume. As visible in Fig. 8(b) the interference pattern was found to have an influence of the velocity profiles and preferably should be prevented, such as with a non-reflective coating outside of the immediate field of view.

4.2. Wall shear stress distribution and statistics

Following Eq. 1 the unsteady wall shear stress (WSS) estimates are directly calculated using the particle's current velocity u_i and distance from the wall Δy_i. Probability distributions of both components of the WSS vector are given in Fig. 9 and closely match those obtained from DNS (see e.g. Fig.5 in Diaz-Daniel et al., 2017). The data are obtained from 60 s of raw data and are sampled in a wall distance of 50-150 µm ($\approx 1.5\,y^+$). The statistics represent a total of 8000 eddy turn-over times of $\delta_{99}/U_e = 7.5$ ms ($\mathrm{Re}_\tau = 563$, $\delta_{99} = 39\,\mathrm{mm}$).

The skewness S_{τ_x} and flatness F_{τ_x} of the WSS components are in good agreement with data obtained by DNS at similar Reynolds numbers (e.g. Table I in Diaz-Daniel et al., 2017). The correlations for $\vec{\tau}_w$ as proposed by Örlü & Schlatter (2011)

$$\tau^+_{x_i,rms} = \frac{\tau_{x_i,rms}}{\tau_w} = C_{0,i} + 0.018\ln \mathrm{Re}_\tau \tag{3}$$

with $C_{0,x} = 0.298$ and $C_{0,z} = 0.164$ respectively predict $\tau^+_{x,rms} = 0.413$ and $\tau^+_{z,rms} = 0.279$.

The WSS estimates are very sensitive to the range of wall distances from which the velocity data and corresponding particle-wall distances are sampled. The WSS fluctuation estimates presented in Fig. 10 are compiled from a variety of recording at different seeding concentration and different sampling intervals.

Whereas the streamwise WSS fluctuations $\tau^+_{x,rms}$ are slightly overestimated, but within error bounds, the spanwise fluctuations $\tau^+_{z,rms}$ are underestimated by more than 10%. A possible explanation for this underestimation will be given in the discussion section.

Finally, 2d probability distributions of the WSS are plotted in Fig. 11 for two Reynolds numbers using a sample size of up to $N = 2 \times 10^7$ (at $\mathrm{Re}_\tau = 563$). These distributions agree very well with the results obtained with multiple-aperture micro-PTV (MA-$upmu$PTV) at the same Reynolds

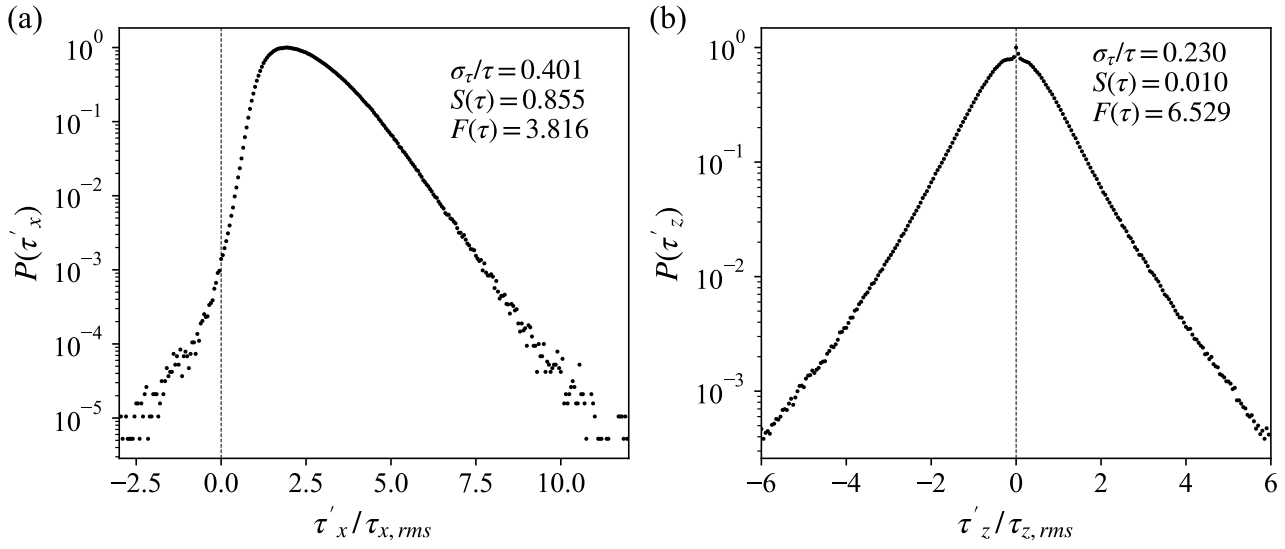

Figure 9. PDFs of streamwise (a) and spanwise (b) wall shear stress components normalized by the rms of the respective values compiled from $1 \cdot 10^7$ correlated samples obtained from an event-record of 60 s duration at $U_\infty = 5.2\,\mathrm{m/s}$ ($\mathrm{Re}_\tau = 563$). Velocity is sampled in the range $0.5 < y^+ < 2.0$.

numbers (see Klinner & Willert, 2024). Similar data has also been acquired by Sheng et al. (2008) for turbulent channel water flow at a friction Reynolds number of $\mathrm{Re}_\tau = 1400$. The contours in Fig. 11 show a small bulge near $\tau_w = 0$, especially for the higher Reynolds number, which is believed to be caused by artefacts arising by the colinear arrangement of the three cameras along the streamwise direction. Due to this linear camera arrangement the epipolars between all three cameras are parallel. Therefore, multiple particles moving in streamwise direction have a higher likelihood of overlapping along the field of view and result in mismatching (ghost particles). More sophisticated LPT schemes, such as a modified 3d STB (Schanz et al., 2016), should be able to handle this deficiency and could potentially recover more tracks from the raw event-data. Adding a fourth camera would also reduce the likelihood of mismatch.

5. Discussion

The estimation of the wall shear stress τ_w based on the discrete approximation given in Eq. 1 is affected by two primary sources of error: (1) the uncertainty of the distance of the particle from the wall ϵ_y and (2) the measurement uncertainty in the particle's velocity ϵ_u. In addition, the approximation Eq. 1 is only valid in the linear range of the velocity profile. At wall distance of $y^+ = 5$ the velocity profile already deviates by nearly $4\,\%$ from linearity. This is illustrated in Fig. 12 for direct numerical simulation (DNS) TBL data at different Reynolds numbers. Therefore, a reliable estimation relies on particle velocity data provided for $y^+ \leq 4$. At the same time, the uncertainty increases nonlinearly as the particle distance Δy approaches the wall while the relative error of the

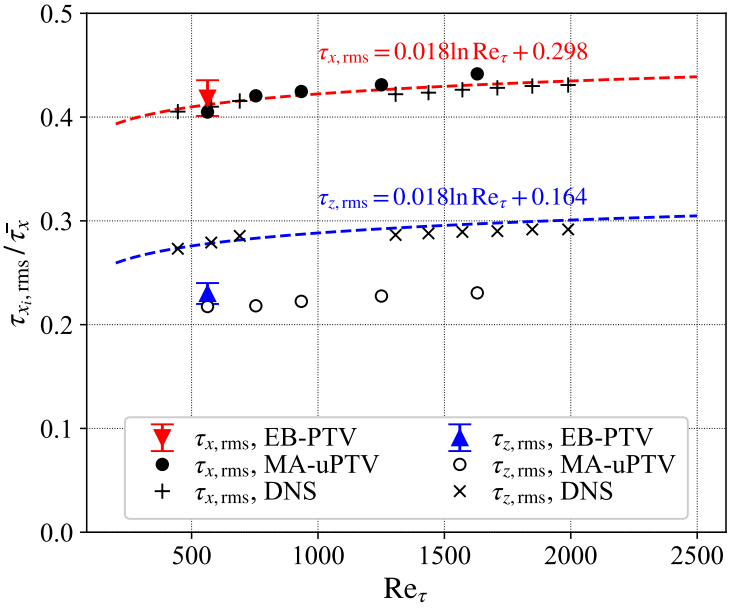

Figure 10. rms fluctuations of WSS of streamwise (▼) and spanwise (▲) components of the WSS, determined from particle tracks in the viscous sub-layer in $0.5 < y^+ < 2.5$. Round markers (•, ○) represent data obtained with MA-μPTV (Klinner & Willert, 2024); TBL-DNS by Sillero et al. (2013). Dashed lines correspond to Eq. 4.2 with different offsets C_i.

velocity increases as well, due to its linear decay toward the no-slip wall. This compounded effect may partially explain the strong deviation of the higher velocity moments, skew S_u and kurtosis F_u for $y^+ < 2$ in Fig. 8c.

The availability of DNS also provides justification for track validation based on the variances of the individual velocity components along the track. In particular, Fig. 13 suggests that, at a wall distance of $y^+ = 4$, wall-normal fluctuations should be about an order of magnitude smaller than streamwise and spanwise fluctuations.

The DNS is particularly helpful in explaining the consistent underestimation of the spanwise WSS fluctuation $\tau^+_{z,rms}$, which not only was observed in the present application, but also in related measurements using highly accurate micro particle tracking techniques by Kumar et al. (2021) and Klinner & Willert (2024). Fig. 13(a) provides profiles of the velocity fluctuations for all 3 velocity components. Focusing in on the near-wall region ($y^+ < 8$) in Fig. 13(b) they are characterized by different rates of change, with u^+_{rms} to strongest, followed by spanwise w^+_{rms} ($\approx 40\%$ at $y^+ = 5$) an wall-normal v^+_{rms} ($\approx 10\%$ at $y^+ = 5$). However, when these quantities are normalized with the mean streamwise velocity U (Fig. 13c), they exhibit a completely different behavior: while the quantity u_{rms}/U shows gradual decrease, its spanwise counterpart w_{rms}/U rapidly decreases with increasing wall distances, whereas the wall-normal quantity gradually increases from 0 at the wall. The limiting values of the former two quantities, u_{rms}/U and w_{rms}/U at the wall ($y = 0$), in fact, coincide with the WSS fluctuations and represent the DNS-based estimates in Fig. 10. In the context of velocimetry-based WSS estimation, the velocity must be sampled at a finite distance Δy from the wall. Close to the wall, both the velocity and wall-distance approach zero and relative errors

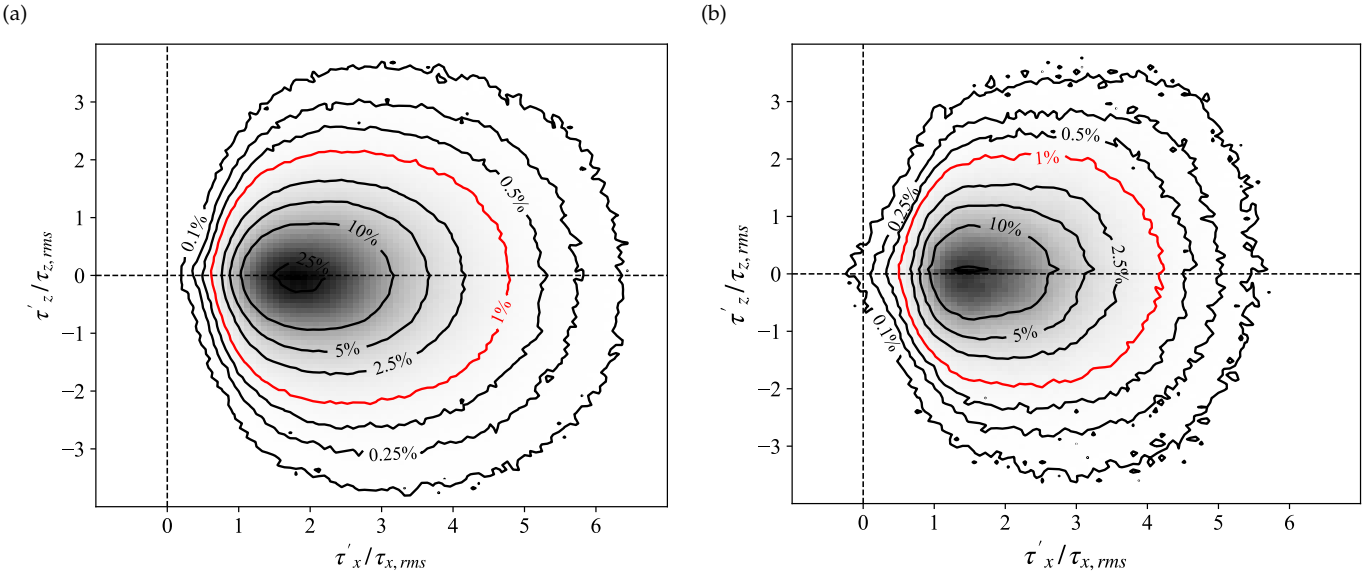

Figure 11. 2d PDFs of the wall shear stress vector normalized by the rms of the respective components compiled from up to $2 \cdot 10^7$ correlated samples from 60 s of raw event data obtained at $U_\infty = 5.2\,\mathrm{m/s}$ ($\mathrm{Re}_\tau = 563$, (a)) and $U_\infty = 7.5\,\mathrm{m/s}$, ($\mathrm{Re}_\tau = 795$, (a)). Contour levels represent probabilities of 0.1%, 0.25%, 0.5%, 1% (red), 2.5%, 5%, 10%, 25%.

rapidly increase. Since the quantity u_{rms}/U has a weaker decay compared to w_{rms}/U, the latter will always be underestimated to a much higher degree. This is illustrated in Fig. 14 by sampling the DNS data at a finite wall distance of $y^+ = 2$, indicated by the black symbols. This sampling domain is comparable to that chosen for the WSS estimation in the present work. The spanwise fluctuation $\tau_{z,\mathrm{rms}}$ obtained with EB–PTV clearly lines up with the predicted estimates from the DNS. If principle the under-estimation can be corrected by computing the velocity variances at different wall-distance intervals and extrapolating the trend toward the wall.

At the highest bulk velocity of $U_\infty = 10\,\mathrm{m/s}$ the particle tracking yield was insufficient for reliable WSS estimation, in part, due to the nearly doubled mean particle displacement (compared to $U_\infty = 5.2\,\mathrm{m/s}$), but also, because of the proportional reduction of the viscous scale from $\nu/u_\tau = 66\,\mu\mathrm{m}$ to $\nu/u_\tau = 37\,\mu\mathrm{m}$. To a certain extent, a proportionally higher laser pulsing frequency could improve the measurement. However, the bandwidth limitation of the EBV camera hardware imposes a limit of about $10\,\mathrm{kHz}$, in particular, at increased seeding levels. Overall it was found that the data quality improves with reduced seeding density which is related to the improved particle matching using only 3 cameras. Adding a fourth camera in the setup would provide additional redundancy, stabilizing the 3d particle position reconstruction.

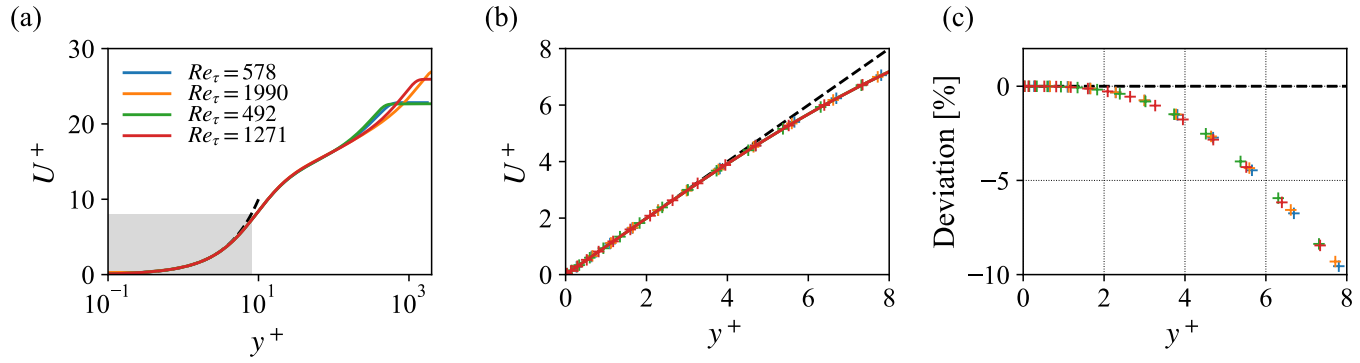

Figure 12. Mean streamwise velocity profiles from DNS of TBLs by Sillero et al. (2013) and Schlatter & Örlü (2010) in log-scaling (a), linear scaling in near the wall (b) and deviation of velocity U^+ from linearity (c). Gray shaded area in (a) represents domain in (b).

6. Conclusion & Outlook

The material presented herein demonstrates the viability of event-based imaging velocimetry for accurate measurement of TBL properties, such as near-wall velocity profiles or wall shear stress (WSS) distributions. The reduced data stream of EBV permits continuous recording on the order of minutes or longer using off-the-shelf computer systems. Uncertainties arising from the limited (1-bit) signal depth of the image data are accounted for by making use of the available temporal resolution of the raw data which is on the order of $10\,\mathrm{kHz}$. Track reconstruction can be greatly improved using Wiener or Kalman filtering such as implemented by Borer et al. (2017) and AlSattam (2024).

Even without processing, the raw event-data is well suited for the visualization of the near wall dynamics. While this is also possible with high-speed particle imaging approaches, the inherent binary nature of the imagery captured by event cameras immediately provides high contrast visualizations without further effort. In the present application, rapid spanwise modulations imposed by the passage of flow structures in the outer layers of the TBL are clearly visualized and suggest further spatio-temporal analysis of the dynamics.

The time-resolved data presented herein was acquired using hardware that is considerably cheaper in comparison to conventional high-speed particle image velocimetry (PIV) components. Beyond this, the higher sensitivity of the EBV detectors reduce the power requirements of the laser used to illuminate the tracer particles.

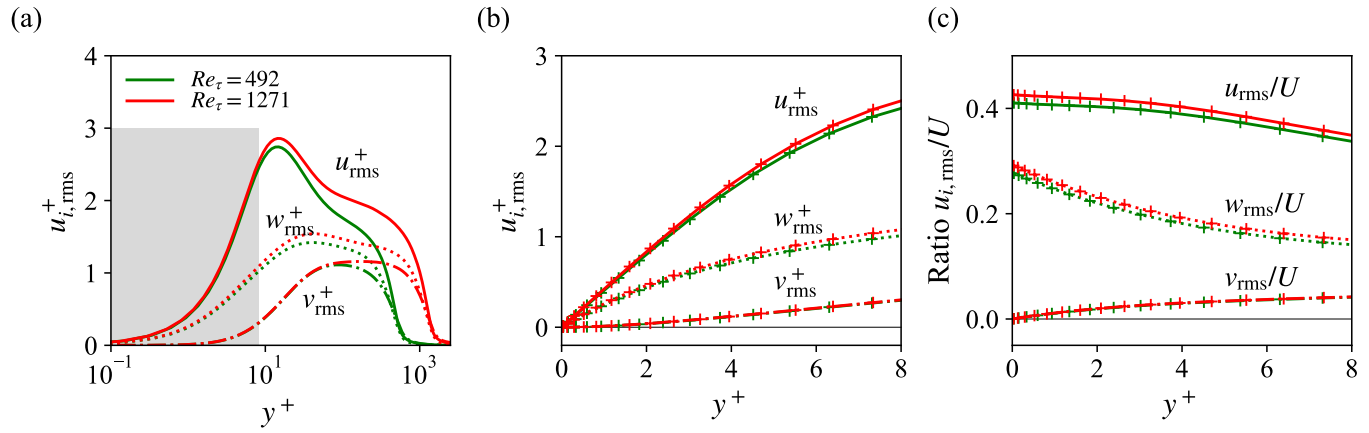

Figure 13. Profiles of root mean square (rms) of streamwise u, wall-normal v and spanwise w velocity from DNS of TBLs by Sillero et al. (2013) in log-scaling (a), linear scaling in near the wall (b) and normalized with mean streamwise velocity U^+ (c). Gray shaded area in (a) represents domain in (b).

Acknowledgments

We are very appreciative of the support by our colleagues of DLR Institute of Aerodynamics and Flow Technology during our measurement campaign in Göttingen, in particular Prof. Markus Raffel and his team for the use of the wind tunnel facility and Prof. Andreas Schröder for providing the high-speed cameras.

References

AlSattam, O. A. (2024). *Noise robust particle event velocimetry with a kalman filter-based tracking* (PhD thesis, University of Dayton, Dayton, Ohio). Retrieved from `http://rave.ohiolink.edu/etdc/view?acc_num=dayton1714134260767049`

Borer, D., Delbruck, T., & Rösgen, T. (2017). Three-dimensional particle tracking velocimetry using dynamic vision sensors. *Experiments in Fluids*, *58*(165). doi: 10.1007/s00348-017-2452-5

Diaz-Daniel, C., Laizet, S., & Vassilicos, J. C. (2017). Wall shear stress fluctuations: Mixed scaling and their effects on velocity fluctuations in a turbulent boundary layer. *Physics of Fluids*, *29*(5), 055102. doi: 10.1063/1.4984002

Drazen, D., Lichtsteiner, P., Haefliger, P., Delbruck, T., & Jensen, A. (2011). Toward real-time particle tracking using an event-based dynamic vision sensor. *Experiments in Fluids*, *51*(1), 1465-1469. Retrieved from `http://www.zora.uzh.ch/60624/1/Drazen_EIF_2011.pdf` doi: 10.1007/s00348-011-1207-y

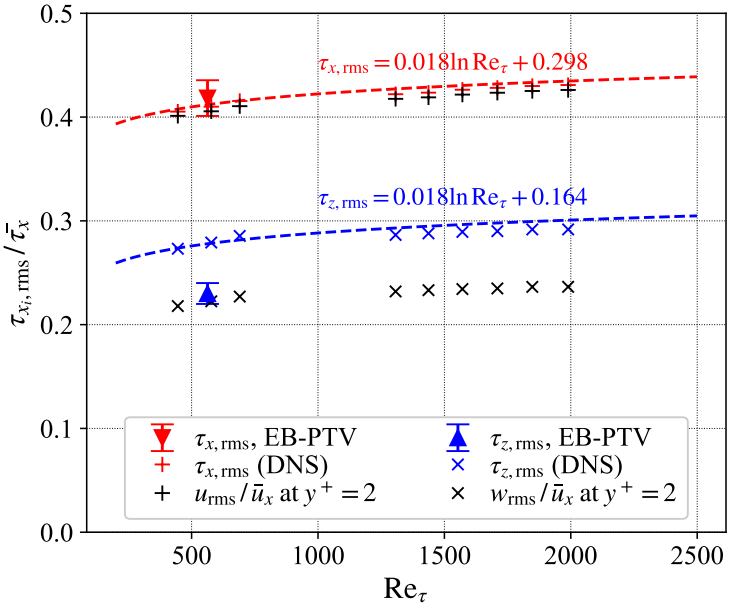

Figure 14. rms fluctuations of WSS components as shown in Fig. 10 but with fluctuations additionally estimated from DMS mean and rms $y^+ = 2.0$ as indicated in Fig. 13(c).

Gallego, G., Delbrück, T., Orchard, G., Bartolozzi, C., Taba, B., Censi, A., ... Scaramuzza, D. (2022). Event-based vision: A survey. *IEEE Transactions on Pattern Analysis and Machine Intelligence*, *44*(1), 154-180. doi: 10.1109/TPAMI.2020.3008413

Klinner, J., & Willert, C. (2024). Wall shear stress characteristics of a turbulent channel boundary layer obtained with multi-aperture defocusing µPTV and high-speed stereo profile-piv. In *21st international symposium on application of laser and imaging techniques to fluid mechanics.* Lisbon, Portugal. Retrieved from `https://elib.dlr.de/204533/`

Kumar, S. S., Huang, X., Yang, X., & Hong, J. (2021). Three dimensional flow motions in the viscous sublayer. *Theoretical and Applied Mechanics Letters*, *11*(2), 100239. Retrieved from `https://doi.org/10.1016/j.taml.2021.100239` doi: 10.1016/j.taml.2021.100239

Ni, Z., Pacoret, C., Benosman, R., Ieng, S., & Régnier, S. (2012). Asynchronous event-based high speed vision for microparticle tracking. *Journal of Microscopy*, *245*(3), 236-244. Retrieved from `https://www.neuromorphic-vision.com/public/publications/14/publication.pdf` doi: 10.1111/j.1365-2818.2011.03565.x

Örlü, R., & Schlatter, P. (2011). On the fluctuating wall-shear stress in zero pressure-gradient turbulent boundary layer flows. *Physics of Fluids*, *23*(2), 021704. doi: 10.1063/1.3555191

Robotics and Perception Group. (2023). *Event-based vision resources.* `https://github.com/uzh-rpg/event-based_vision_resources`. GitHub.

Rusch, A., & Rösgen, T. (2023). TrackAER: real-time event-based quantitative flow visualization. *Experiments in Fluids*, *64*, 136. Retrieved from https://doi.org/10.1007/s00348-023-03673-0 doi: 10.1007/s00348-023-03673-0

Schanz, D., Gesemann, S., & Schröder, A. (2016). Shake-The-Box: Lagrangian particle tracking at high particle image densities. *Experiments in Fluids*, *57*(5), 1-27. Retrieved from http://dx.doi.org/10.1007/s00348-016-2157-1 doi: 10.1007/s00348-016-2157-1

Schlatter, P., & Örlü, R. (2010). Assessment of direct numerical simulation data of turbulent boundary layers. *Journal of Fluid Mechanics*, *659*, 116–126. doi: 10.1017/S0022112010003113

Sheng, J., Malkiel, E., & Katz, J. (2008). Using digital holographic microscopy for simultaneous measurements of 3d near wall velocity and wall shear stress in a turbulent boundary layer. *Experiments in Fluids*, *45*, 1023–1035. Retrieved from https://doi.org/10.1007/s00348-008-0524-2 doi: 10.1007/s00348-008-0524-2

Sillero, J. A., Jiménez, J., & Moser, R. D. (2013). One-point statistics for turbulent wall-bounded flows at Reynolds numbers up to $\delta^+ \approx 2000$. *Physics of Fluids*, *25*(10), 105102. Retrieved from http://aip.scitation.org/doi/10.1063/1.4823831 doi: 10.1063/1.4823831

Wang, Y., Idoughi, R., & Heidrich, W. (2020). Stereo event-based particle tracking velocimetry for 3d fluid flow reconstruction. In A. Vedaldi, H. Bischof, T. Brox, & J.-M. Frahm (Eds.), *Computer vision - eccv 2020* (p. 36-53). Cham: Springer International Publishing. Retrieved from https://www.ecva.net/papers/eccv_2020/papers_ECCV/papers/123740035.pdf doi: 10.1007/978-3-030-58526-6_3

Willert, C. (2023). Event-based imaging velocimetry using pulsed illumination. *Experiments in Fluids*, *64*. doi: 10.1007/s00348-023-03641-8

Willert, C., & Klinner, J. (2022). Event-based imaging velocimetry: An assessment of event-based cameras for the measurement of fluid flows. *Experiments in Fluids*, *63*. doi: 10.1007/s00348-022-03441-6